9th International Conference on Numerical Ship Hydrodynamics
Ann Arbor, Michigan, August 5-8, 2007

An Application of Cartesian-Grid and Volume-of-Fluid Methods to Numerical Ship Hydrodynamics

Douglas G. Dommermuth[1], Thomas T. O'Shea[1], Donald C. Wyatt[1],
Toby Ratcliffe[2], Gabriel D. Weymouth[3], Kelli L. Hendrikson[3], Dick K.P. Yue[3],
Mark Sussman[4], Paul Adams[5], and Miguel Valenciano[5]

[1]Naval Hydrodynamics Division, Science Applications International Corporation,
10260 Campus Point Drive, MS 35, San Diego, CA 92121

[2]Carderock Division, Naval Surface Warfare Center, West Bethesda, MD 20817

[3]Department of Mechanical Engineering, Massachusetts Institute of Technology, Cambridge, MA 02139

[4]Department of Mathematics, Florida State University, Tallahassee, FL 32306

[5]U.S. Army Engineer Research and Development Center, Vicksburg, MS 39180

Abstract

A combination of cartesian-grid methods and volume-of-fluid methods is used to simulate breaking waves around ships and the resulting hydrodynamic forces. A surface panelization of a ship hull is used as input to automatically generate an immersed-boundary representation of the geometry on a cartesian grid. No additional gridding beyond what is already used in potential-flow methods and hydrostatics calculations is required. The volume-of-fluid portion of the numerical algorithm is used to capture the free-surface interface, including the breaking of waves, the formation of spray, and the entrainment of air. The numerical scheme is implemented on a parallel computer. The numerical simulations are compared to analytical solutions and experimental measurements. Together, the ease of input and usage, the ability to model and resolve complex free-surface phenomena, and the speed of the numerical algorithm provide a robust capability for simulating the free-surface disturbances near a ship.

Introduction

The Numerical Flow Analysis (NFA) code provides turnkey capabilities to model breaking waves around a ship, including both plunging and spilling breaking waves, the formation of spray, and the entrainment of air. The basic details of the numerical algorithm are provided in Sussman & Dommermuth (2001), and Dommermuth et al. (2004), and Dommermuth et al. (2006). An evaluation of NFAs capabilities is provided in Wilson et al. (2006). Here, the numerical formulation of NFA will be discussed in detail, including the treatment of the hull boundary condition and the update of the free-surface elevation. The calculation of hydrodynamic forces and the modeling of nonlinear incident waves will be used to illustrate the accuracy and stability of the numerical formulation.

NFA uses a cartesian-grid formulation with immersed-body and volume-of-fluid (VOF) methods. The governing equations are formulated on a cartesian grid thereby eliminating complications associated with body-fitted grids. The sole geometric input into NFA is a surface panelization of the ship hull. No additional gridding beyond what is already used in potential-flow methods and hydrostatics calculations is required. The ease of input in combination with a flow solver that is implemented using parallel-computing methods permit the rapid turn around of numerical simulations of complex interactions between free surfaces and ships.

Based on Colella et al. (1999) and Sussman & Dommermuth (2001), free-slip boundary conditions are imposed on the surface of the ship hull. A surface representation of the ship hull is used as input to construct a three-dimensional signed-distance representation. The signed-distance function is used to calculate how the ship hull cuts through the cartesian grid. The resulting fractional areas and volumes are then used in a finite-volume method to project the flow velocity onto a solenoidal field and to impose the hull boundary conditions. The fractional areas and volumes of very small cells are merged to improve the conditioning of the Poisson solver (Mampaey & Xu 1995). Free-slip boundary conditions are also imposed along the sides and at the top and bottom of the computational domain. At the exit, Orlanski-like boundary conditions are imposed (Orlanski 1976). At the entrance, a wavemaker is used to generate ambient waves. The ambient waves are accurate to second order in wave steepness. The water-particle velocity in the water and air, and the free-surface elevation is assigned at the entrance to the computational domain.

The grid is stretched along the cartesian axes using one-dimensional elliptic equations to improve resolution near the ship hull and the free-surface interface. Away

from the ship and the free-surface interface, where the flow is less complicated, the mesh is coarser. Details of the grid stretching algorithm, which uses weight functions that are specified in physical space, are provided in Knupp & Steinerg (1993).

The VOF portion of the numerical algorithm is used to track the free-surface interface, including the large-scale effects of breaking waves, spray formation and air entrainment. The interface tracking of the free surface is second-order accurate in space and time. At each time step, the position of the free surface is reconstructed using piece-wise planar surfaces (Rider et al. 1994, Gueyffier et al. 1999). The advection portion of the VOF algorithm uses an operator-split method (Puckett et al. 1997). The advection algorithm implements a correction to improve mass conservation when the flow is not solenoidal due to numerical errors.

The convective terms in the momentum equations are treated using a slope-limited, third-order QUICK scheme as discussed in Leonard (1997). A Smagorinsky turbulence model is also implemented. There are no special treatments required to model either the flow separation at the transom or the wave overturning at the bow. A second-order, variable-coefficient Poisson equation is used to project the velocity onto a solenoidal field. A preconditioned conjugate-gradient method is used to solve the Poisson equation.

NFA is written in Fortran 90. The governing equations are solved using a domain-decomposition method. The domains are distributed over the nodes of a parallel computer. Communication between processors on the Cray XT3 is performed using either Crays shared memory access library (SHMEM). NFA also runs on clusters using MPI. The CPU requirements are linearly proportional to the number of grid points and inversely proportional to the number of processors. Together, the ease of input and usage, the ability to model and resolve complex free-surface phenomena, and the speed of the numerical algorithm provide a robust capability for simulating the free-surface disturbances near a ship.

Formulation

Consider turbulent flow at the interface between air and water. A two-phase formulation of the Navier-Stokes equations is used to model a ship moving with constant forward speed with incident waves. Let u_i denote the three-dimensional velocity field as a function of space ($x_i = (x, y, z)$) and time (t). v_i is the velocity of the ship. v_i includes the effects of rigid-body translation and rotation. Let U_i denote the free-stream current. For an incompressible flow, the conservation of mass gives

$$\frac{\partial u_i}{\partial x_i} = 0 \quad . \tag{1}$$

u_i and x_i are normalized by U_o and L_o, which denote the free-stream velocity and the length of the body, respectively. The frame of reference is fixed with respect to the initial position of the ship's fore perpendicular. A right-handed coordinate system is used with x positive forward and z positive upward.

Following a procedure that is similar to Rider et al. (1994), we let ϕ denote the fraction of fluid that is inside a cell. By definition, $\phi = 0$ for a cell that is totally filled with air, and $\phi = 1$ for a cell that is totally filled with water.

The advection of ϕ is expressed as follows:

$$\frac{\partial \phi}{\partial t} + \frac{\partial}{\partial x_j}\left[(u_j + U_j)\phi\right] = \frac{\partial Q}{\partial x_j} \quad , \tag{2}$$

Q is a sub-grid-scale flux which can model the entrainment of gas into the liquid. Dommermuth et al. (1998) provide details of a sub-grid model that is appropriate for interface capturing methods that allow mixing of air and water. $Q = 0$ for the present formulation.

Let ρ_ℓ and μ_ℓ respectively denote the density and dynamic viscosity of water. Similarly, ρ_g and μ_g are the corresponding properties of air. The flows in the water and the air are governed by the Navier-Stokes equations:

$$\begin{aligned} \frac{du_i}{dt} + \frac{\partial}{\partial x_j}\left[(u_j + U_j)u_i\right] &= -\frac{1}{\rho}\frac{\partial P}{\partial x_i} \\ &+ \frac{1}{\rho R_e}\frac{\partial}{\partial x_j}\left(2\mu S_{ij}\right) - \frac{\delta_{i3}}{F_r^2} + \frac{\partial \tau_{ij}}{\partial x_j} \quad , \end{aligned} \tag{3}$$

where $R_e = \rho_\ell U_o L_o/\mu_\ell$ is the Reynolds number and $F_r^2 = U_o^2/(gL_o)$ is the Froude number. g is the acceleration of gravity. δ_{i3} is the Kronecker delta function. P is the pressure. As described in Dommermuth et al. (1998), τ_{ij} is the subgrid-scale stress tensor. S_{ij} is the deformation tensor:

$$S_{ij} = \frac{1}{2}\left(\frac{\partial u_i}{\partial x_j} + \frac{\partial u_j}{\partial x_i}\right) \quad . \tag{4}$$

ρ and μ are respectively the dimensionless variable densities and viscosities:

$$\begin{aligned} \rho(\phi) &= \lambda + (1-\lambda)\mathrm{H}(\phi) \\ \mu(\phi) &= \eta + (1-\eta)\mathrm{H}(\phi) \quad , \end{aligned} \tag{5}$$

where $\lambda = \rho_g/\rho_\ell$ and $\eta = \mu_g/\mu_\ell$ are the density and viscosity ratios between air and water. For a sharp interface, with no mixing of air and water, H is a step function. In practice, a mollified step function is used to provide a smooth transition between air and water.

A no-flux condition is imposed on the surface of the ship hull:

$$u_i n_i + U_i n_i = v_i n_i \tag{6}$$

where n_i denotes the normal to the ship hull that points into the fluid.

As discussed in Dommermuth et al. (1998), the divergence of the momentum equations (3) in combination with the conservation of mass (1) provides a Poisson equation for the dynamic pressure:

$$\frac{\partial}{\partial x_i}\frac{1}{\rho}\frac{\partial P}{\partial x_i} = \Sigma \ , \tag{7}$$

where Σ is a source term. As shown in the next section, the pressure is used to project the velocity onto a solenoidal field.

NUMERICAL TIME INTEGRATION

Based on Sussman (2003a), a second-order Runge-Kutta scheme is used to integrate with respect to time the field equations for the velocity field. Here, we illustrate how a volume of fluid formulation is used to advance the volume-fraction function. Similar examples are provided by Rider et al. (1994). During the first stage of the Runge-Kutta algorithm, a Poisson equation for the pressure is solved:

$$\frac{\partial}{\partial x_i}\frac{1}{\rho(\phi^k)}\frac{\partial P^k}{\partial x_i} = \frac{\partial}{\partial x_i}\left(\frac{u_i^k}{\Delta t} + R_i\right) \ , \tag{8}$$

where R_i denotes the nonlinear convective, hydrostatic, viscous, and sub-grid-scale terms in the momentum equations. u_i^k, ρ^k, and P^k are respectively the velocity components, density, and pressure at time step k. Δt is the time step.

For the next step, this pressure is used to project the velocity onto a solenoidal field. The first prediction for the velocity field (u_i^*) is

$$u_i^* = u_i^k + \Delta t\left(R_i - \frac{1}{\rho(\phi^k)}\frac{\partial P^k}{\partial x_i}\right) \tag{9}$$

The volume fraction is advanced using a volume of fluid operator (VOF):

$$\phi^* = \phi^k - \text{VOF}\left(u_i^k, \phi^k, \Delta t\right) \tag{10}$$

Details of the VOF operator are provided later. A Poisson equation for the pressure is solved again during the second stage of the Runge-Kutta algorithm:

$$\frac{\partial}{\partial x_i}\frac{1}{\rho(\phi^*)}\frac{\partial P^*}{\partial x_i} = \frac{\partial}{\partial x_i}\left(\frac{u_i^* + u_i^k}{\Delta t} + R_i\right) \tag{11}$$

u_i is advanced to the next step to complete one cycle of the Runge-Kutta algorithm:

$$u_i^{k+1} = \frac{1}{2}\left(u_i^* + u_i^k + \Delta t\left(R_i - \frac{1}{\rho(\phi^*)}\frac{\partial P^*}{\partial x_i}\right)\right) \ , \tag{12}$$

and the volume fraction is advanced to complete the algorithm:

$$\phi^{k+1} = \phi^k - \text{VOF}\left(\frac{u_i^* + u_i^k}{2}, \phi^k, \Delta t\right) \tag{13}$$

GRIDDING

Along the cartesian axes, one-dimensional stretching is performed using a differential equation. Let x denote the position of the grid points in physical space, and let ξ denote the position of the grid points in a mapped space. As shown by Knupp & Steinerg (1993), the differential equation that describes grid stretching in one dimension is as follows:

$$\frac{\partial^2 x}{\partial \xi^2} + \frac{1}{w}\frac{\partial w}{\partial \xi}\frac{\partial x}{\partial \xi} = 0 \ , \tag{14}$$

where $w(x)$ is a weight function that is specified in physical space. For example, suppose the grid spacing is constant but different for $x < x_o$ and $x > x_1$. Between $x_o \le x \le x_1$, there is a transition zone from one grid spacing to the next. Then the following weight function may be used to describe this distribution of grid points:

$$\begin{aligned} w(x) &= w_0 \ \text{ for } \ x < x_0 \\ w(x) &= \frac{w_0 - w_1}{2}\left(1 + \cos(\pi\frac{x - x_0}{x_1 - x_0})\right) \\ &+ w_1 \ \text{ for } \ x_0 \le x \le x_1 \\ w(x) &= w_1 \ \text{ for } \ x > x_1 \ . \end{aligned} \tag{15}$$

Using this approach, multiple zones of grid clustering may be specified. For example, along the x-axis (x_1 in indical notation), grid points may be clustered near the bow and stern. For the y-axis (x_2 in indical notation), grid points are clustered near the centerline out beyond the half beam. Finally, for the z-axis (x_3 in indical notation), grid points are clustered near the mean waterline in a region that is between the top and bottom of the ship hull. Note that equation 14, is a nonlinear equation that is solved iteratively.

ENFORCEMENT OF BODY BOUNDARY CONDITIONS

A no-flux boundary condition is imposed on the surface of the body using a finite-volume technique. A signed distance function ψ is used to represent the body. ψ is positive outside the body and negative inside the body. The magnitude of ψ is the minimal distance between the position of ψ and the surface of the body. ψ is zero on the surface of the body. ψ is calculated using a surface panelization of the hull form. Green's theorem is used to indicate whether a point is inside or outside the body, and then the shortest distance from the point to the surface of the body is calculated. Triangular panels are

used to discretize the surface of the body. The shortest distance to the surface of the body can occur on either a surface, edge, or vertice of a triangular panel. Details associated with the calculation of ψ are provided in Sussman & Dommermuth (2001).

Cells near the ship hull may have an irregular shape, depending on how the surface of the ship hull cuts the cell. On these irregular boundaries, the finite-volume approach is used to impose free-slip boundary conditions. Let S_b denote the portion of the cell whose surface is on the body, and let S_o denote the other bounding surfaces of the cell that are not on the body. Gauss's theorem is applied to the volume integral of equation 8:

$$\int_{S_o+S_b} ds \frac{n_i}{\rho(\phi^k)} \frac{\partial P^k}{\partial x_i} = \int_{S_o+S_b} ds \left(\frac{u_i^k n_i}{\Delta t} + R_i n_i \right) . \quad (16)$$

Here, n_i denotes the components of the unit normal on the surfaces that bound the cell. Based on equation 9, a Neumann condition is derived for the pressure on S_b as follows:

$$\frac{n_i}{\rho(\phi^k)} \frac{\partial P^k}{\partial x_i} = -\frac{u_i^* n_i}{\Delta t} + \frac{u_i^k n_i}{\Delta t} + R_i n_i \quad . \quad (17)$$

The Neumann condition for the velocity (6) is substituted into the preceding equation to complete the Neumann condition for the pressure on S_b:

$$\frac{n_i}{\rho(\phi^k)} \frac{\partial P^k}{\partial x_i} = \frac{U_i^* n_i}{\Delta t} - \frac{v_i^* n_i}{\Delta t} + \frac{u_i^k n_i}{\Delta t} + R_i n_i \quad . \quad (18)$$

This Neumann condition for the pressure is substituted into the integral formulation in equation 16:

$$\begin{aligned} \int_{S_o} ds \frac{1}{\rho(\phi^k)} \frac{\partial P^k}{\partial x_i} n_i &= \int_{S_o} ds \left(\frac{u_i^k n_i}{\Delta t} + R_i n_i \right) \\ &+ \int_{S_b} ds (v_i^* - U_i^*) \frac{n_i}{\Delta t} . \quad (19) \end{aligned}$$

This equation is solved using the method of fractional areas. Details associated with the calculation of the area fractions are provided in Sussman & Dommermuth (2001) along with additional references. Cells whose cut volume is less than 25% of the full volume of the cell are merged with neighbors. The merging occurs along the direction of the steepest gradient of the signed-distance function ψ. This improves the conditioning of the Poisson equation for the pressure. As a result, the stability of the projection operator for the velocity is also improved (see equations 9 and 12).

As the ship moves due to force motions or in response to incident waves, the signed-distance function ψ and the fractional areas and volumes are recalculated each time step. In the case of forced motions, the signed-distance function can be precalculated over the range of motion, then interpolation can be used during the simulation to calculate the signed-distance function to improve efficiency.

INTERFACE RECONSTRUCTION AND ADVECTION

In our VOF formulation, the free surface is reconstructed from the volume fractions using piece-wise linear polynomials. The reconstruction is based on algorithms that are described by Gueyffier et al. (1999). The surface normals are estimated using weighted central differencing of the volume fractions. A similar algorithm is described by Pilliod & Puckett (1997). Near the body, care must be taken to use cells whose volume fraction is exterior to the body in the calculation of the normal to the free-surface interface. The advection portion of the algorithm is operator split, and it is based on similar algorithms reported in Puckett et al. (1997). Major differences between the present algorithm and earlier methods include special treatments to account for the body and to alleviate mass-conservation errors due to the presence of non-solenoidal velocity fields.

Let F_i denote flux through the faces of a cell. F_i is expressed in terms of the relative velocity $(u_i + U_i - v_i)$ and the areas of the faces of the cell (A_i) that are cut by the ship hull:

$$F_i = A_i \left(u_i + U_i - v_i \right) \quad . \quad (20)$$

If the ship hull does not cut the cell, then A_i correspond to the surface areas that bound the cell. Near the ship hull, A_i is some fraction of the surface areas that bound the cell. Note that $A_i = 0$ inside the ship hull. Based on an application of Gauss's theorem to the volume integral of Equation 1 and making use of Equation 6:

$$F_i^+ - F_i^- = 0 \quad , \quad (21)$$

where F_i^+ is the flux on the positive i-th face of the cell and F_i^- is the flux on the negative i-th face of the cell. Due to numerical errors, equation 21 is not necessarily satisfied. Let $\mathcal{E}$ denote the resulting numerical error for any given cell. For each cell whose flux is not conserved, a correction is applied prior to performing the VOF advection. For example, the following reassignment of the flux along the vertical direction ensures that the redefined flux is conserved:

$$\begin{aligned} \tilde{F}_3^+ &= F_3^+ - \frac{\mathcal{E} A_3^+}{A_3^+ + A_3^-} \\ \tilde{F}_3^- &= F_3^- + \frac{\mathcal{E} A_3^-}{A_3^+ + A_3^-} \end{aligned} \quad (22)$$

Based on this new flux, new relative velocities are defined on the faces of the cell:

$$\hat{u}_i = \frac{\Delta x_i \tilde{F}_i}{\mathrm{V}} \quad (23)$$

where Δx_i is the grid spacing and $\mathrm{V} = \Delta x_1 \Delta x_2 \Delta x_3$ is the volume of the cell. Away from the ship hull, $\hat{u}_i$

is the relative velocity plus a corrective term to conserve mass. Inside the ship hull, $\hat{u}_i = 0$ because $A_i = 0$. Near the ship hull, $\hat{u}_i$ is scaled by the fraction of area that is cut by the presence of the ship hull. $\hat{u}_i$ is continuous across the faces of the cells along $x-$ and $y-$axes, but discontinuous across the faces along the $z-$axis because in this particular example that is the axis where the flux has been corrected.

Equation 2 is operator split. A dilation term is added to ensure that the volume fraction remains between $0 \leq \phi \leq 1$ during each stage of the splitting (Puckett et al. 1997). The resulting discrete set of equations for the first stage of the time-stepping procedure is provided below:

$$\begin{aligned}
\tilde{\phi} = \phi^k &- \frac{\mathcal{F}_1\left[\left(\hat{u}_1^+\right)^k, \phi^k, \Delta t\right] - \mathcal{F}_1\left[\left(\hat{u}_1^-\right)^k, \phi^k, \Delta t\right]}{\mathrm{V}} \\
&+ \Delta t \tilde{\phi} \frac{\left(\hat{u}_1^+\right)^k - \left(\hat{u}_1^-\right)^k}{\Delta x_1} \\
\tilde{\tilde{\phi}} = \tilde{\phi} &- \frac{\mathcal{F}_2\left[\left(\hat{u}_2^+\right)^k, \tilde{\phi}, \Delta t\right] - \mathcal{F}_2\left[\left(\hat{u}_2^-\right)^k, \tilde{\phi}, \Delta t\right]}{\mathrm{V}} \\
&+ \Delta t \tilde{\tilde{\phi}} \frac{\left(\hat{u}_2^+\right)^k - \left(\hat{u}_2^-\right)^k}{\Delta x_2} \\
\phi^* = \tilde{\tilde{\phi}} &- \frac{\mathcal{F}_3\left[\left(\hat{u}_3^+\right)^k, \tilde{\tilde{\phi}}, \Delta t\right] - \mathcal{F}_3\left[\left(\hat{u}_3^-\right)^k, \tilde{\tilde{\phi}}, \Delta t\right]}{\mathrm{V}} \\
&+ \Delta t \tilde{\tilde{\phi}} \frac{\left(\hat{u}_3^+\right)^k - \left(\hat{u}_3^-\right)^k}{\Delta x_3} \quad , \qquad (24)
\end{aligned}$$

$\mathcal{F}_i$ denotes VOF advection based on the uncut areas of the faces of the cell. As an example, for a cell that is full of water, $\mathcal{F}_1(\hat{u}_1, \phi, \Delta t) = \phi \hat{u}_1 \Delta t \Delta x_2 \Delta x_3$. The dilation term is treated explicitly in the first two parts of the operator-split algorithm and implicitly in the last part of the preceding equation. Note that the order of the splitting is alternated from time step to time step to preserve second-order accuracy.

Interface Visualization

The free-surface interface that is reconstructed from the volume fractions is most often calculated and visualized using commercial codes. Specifically, commercial codes calculate the 0.5 isosurface of the volume-fraction function ϕ. The free-surface interface that is calculated from the 0.5 isosurface is different from the free-surface interface that is reconstructed from the volume fractions. To illustrate this point, consider a cell whose volume fraction ϕ_o is between half full and full, $0.5 \leq \phi_o \leq 1$. Let Δz denote the height of the cell. Assume that the free-surface interface is horizontal and that all the fluid is sitting in the bottom of the cell. Then the height of the free-surface interface above the bottom of the cell based on VOF reconstruction is as follows:

$$\eta = \phi_o \Delta z \quad . \qquad (25)$$

In contrast, if the cell above is filled with air. then based on the 0.5 isosurface, the height of the free-surface interface is

$$\eta = \left(\frac{3}{2} - \frac{1}{2\phi_o}\right) \Delta z \quad . \qquad (26)$$

The maximum difference between equations 25 and 26 occurs when $\phi_o = 3/4$. The error at this point is about 11% higher for 0.5 isosurface relative to VOF reconstruction. If the volume fraction is less than $\phi < 0.5$ within a cell and its neighbors, then the 0.5 isosurface does not even exist. This is problematic in visualizations of turbulent flows with lots of spray because droplets and sheets of water can suddenly appear and disappear.

Radiation Conditions

Exit boundary conditions are required in order to conserve mass and flux. For ships with forward speed, an Orlanski-like formulation (Orlanski 1976) provides the necessary radiation condition.

$$\frac{\partial u_1}{\partial t} + U_o \frac{\partial u_1}{\partial x} = 0 \quad . \qquad (27)$$

U_o is the free-stream current along the x-axis, and u_1 is the water-particle velocity along the x-axis. For the other components of velocity and the volume fraction, zero gradients are imposed at the exit of the computational domain:

$$\frac{\partial u_2}{\partial x} = \frac{\partial u_3}{\partial x} = \frac{\partial \phi}{\partial x} = 0 \quad . \qquad (28)$$

Neumman conditions are specified for the pressure in a manner that is very similar to the imposition of free-slip conditions on the ship hull (see equations 16 thru 19). Based on the x-component of momentum,

$$\frac{1}{\rho}\frac{\partial P}{\partial x} = -\frac{\partial u_1}{\partial t} + R_1 \quad . \qquad (29)$$

Upon substitution of equation 27 into the preceding equation, the following Neumann condition is derived for the pressure at the exit of the computational domain:

$$\frac{1}{\rho}\frac{\partial P}{\partial x} = U_o \frac{\partial u_1}{\partial x} + R_1 \quad . \qquad (30)$$

This equation is substituted into the set of finite-volume equations that govern the pressure (see equation 19).

Equations 27 thru 30 prevent the reflection of disturbances back into the interior of the computational domain. However, these equations do not guarantee the

conservation of mass. In order to conserve mass, a regridding procedure is introduced when there are no incident waves. The initial volume fraction is integrated for the grid cells that are on the leading edge of the computational domain. This integrated quantity is used to maintain a constant mean water level at the entrance to the computational domain. At the end of each time step, changes in the integrated volume fraction are calculated. Any changes in the integrated volume fraction are eliminated by imposing a vertical velocity that brings the mean water level at the leading edge back into alignment. The velocity correction is used to move the volume fractions over the entire computational domain either up or down, depending on the situation. A VOF method is used to move the volume fractions. The VOF method ensures that the free-surface interface remains sharp during the regridding process.

INITIAL TRANSIENTS

Initial transients are minimized using an adjustment procedure. An analysis of adjustment procedures as it applies to free-surface problems is provided in Dommermuth (1994) and Dommermuth (2000). Let $f(t)$ denote the adjustment factor as a function of time, then $f(t)$ and its derivative $f'(t)$ are by definition

$$\begin{aligned} f(t) &= 1 - \exp(-(\frac{t}{T_o})^2) \\ f'(t) &= 2\frac{t}{T_o^2}\exp(-(\frac{t}{T_o})^2) \ , \end{aligned} \tag{31}$$

where T_o is the adjustment time.

For a ship hull that is oscillating up and down, the vertical motion (z) and vertical velocity (w) of the ship hull are

$$\begin{aligned} z &= Asin(\omega t)f(t) \\ w &= A\omega\cos(\omega t)f(t) + Asin(\omega t)f'(t) \ . \end{aligned} \tag{32}$$

A is the amplitude and ω is the frequency of the vertical motion. A similar procedure is used for forced roll and pitch motions. The free-stream current is also slowly ramped up to speed.

ENFORCEMENT OF COURANT CONDITIONS

The momentum equations are integrated in time using an explicit Runge-Kutta algorithm. As a result, a Courant condition must be enforced for the maximum total velocity:

$$|u_i + U_i| \leq C\frac{\Delta x_i}{\Delta t} \tag{33}$$

C is a coefficient that ensures that the Courant condition is satisfied for both the momentum equations and the VOF advection. Typically, $C = 0.45$ in the numerical results that are presented in this paper. If the Courant condition is exceeded, the magnitude of the velocity is reduced such that the Courant condition is satisfied. This clipping of the velocity field tends to occur in regions where fine spray is formed, especially in the rooster-tail region.

TREATMENT OF CONVECTIVE TERMS

The convective terms in the momentum equations (see Equation 3) are calculated using a slope-limited, QUICK, finite-difference scheme (Leonard 1997). Special treatments are required near the ship hull. One possibility is to use one-sided differencing. However, one-sided differencing is often unstable. Another possibility is to extend the velocity of the fluid into the ship hull. In this case, setting the velocity equal to zero inside the body is stable, but too "sticky." Another possibility is to extend the fluid velocity into the ship hull in such a manner that the no-flux condition is met right at the ship hull. The interior flow that meets this condition is as follows:

$$u_i = \left[(v_j - U_j)n_j\right]n_i \ , \tag{34}$$

where recall that v_j is velocity of the body, U_i is the velocity of the free-stream current, and n_j is the unit normal that points along gradient of the signed-distance function (ψ). At the ship hull, $u_i n_i = v_i n_i - U_i n_i$ using this formulation of the interior flow.

DENSITY SMOOTHING

The density as a function of the volume fraction is smoothed using a three-point stencil (1/4,1/2,1/4) that is applied consecutively along each of the cartesian axes. This improves the conditioning of the Poisson equation (Equations 8 & 11). If the density is smoothed, then the same smoothed density must be used in the projection steps (Equations 9 & 12).

CALCULATION OF FORCES

The forces F_i acting on the ship hull are calculated in two parts based on integration of the normal and tangential stresses over the surface of the ship.

$$F_i = \int dsPn_i + \int ds\tau_i \ , \tag{35}$$

where the normal stress is expressed in terms of the pressure P, and the tangential stress τ_i is expressed in terms of the water-particle velocity just outside the boundary layer of the ship.

$$\tau_i = c_f\frac{1}{2}\rho|U|(u_i + U_i - v_i) \ , \tag{36}$$

where c_f is the friction coefficient based on the ITTC line.

$$c_f = 0.075(\log(R_e) - 2)^{-2} \quad . \tag{37}$$

$|U|$ is the magnitude of the water-particle velocity.

$$|U| = \sqrt{(u_i + U_i - v_i)(u_i + U_i - v_i)} \quad .$$

Note that $(u_i + U_i - v_i)n_i = 0$. Similarly, the moments M_i are expressed as follows:

$$M_i \quad = \quad \int dsP\epsilon_{ijk} r_j n_k + \int ds\epsilon_{ijk} r_j \tau_k \quad , \tag{38}$$

where ϵ_{ijk} is the Levi-Civita function. r_j is the moment arm and $\epsilon_{ijk} r_j n_k$ is the indicial-notation representaiton of the cross product of the moment arm with the unit normal.

The surface integrals for the forces and moments are calculated using the panelized geometry. The density, pressure, and water-particle velocities are interpolated onto the panels. The integrands are evaluated and summed over the surface of the body.

WAVEMAKER

Here, we highlight the formulation of a wavemaker. Let $\eta(x,t)$ denote the free-surface elevation as function of position x and time t, then

$$\begin{aligned} \eta(x,t) \quad &= \quad af(t)\cos(kx + \sigma t) \\ &+ \quad \frac{a}{2} kaf(t)\cos(2kx + 2\sigma t) \quad , \end{aligned} \tag{39}$$

where a is the wave amplitude, k is the wavenumber, and σ is the encounter frequency. The preceding formula is accurate to second order in wave steepness. $f(t)$ is an adjustment factor that slowly ramps up the wave amplitude (see Equation 31). The encounter frequency is a function of the intrinsic wave frequency ω, the wavenumber, and the speed of the free-stream current U_o :

$$\sigma = \omega - kU_o(t) \quad , \tag{40}$$

where the normalized intrinsic wave frequency is

$$\omega^2 = \frac{k}{F_r^2} \tanh(kd) \quad , \tag{41}$$

where d is the water depth. The speed of the ship is slowly ramped up from rest using the adjustment factor.

$$U_o(t) = -f(t) \quad . \tag{42}$$

For $z \leq \eta$, the horizontal and vertical components of the water-particle velocity are

$$\begin{aligned} u(x,z,t) \quad &= \quad -a\omega f(t) \frac{\cosh(k(z+d))}{\sinh(kd)} \cos(kx + \sigma t) \\ w(x,z,t) \quad &= \quad -a\omega f(t) \frac{\sinh(k(z+d))}{\sinh(kd)} \sin(kx + \sigma t) \quad . \end{aligned} \tag{43}$$

For $z > \eta$, the horizontal and vertical components of the air-particle velocity are

$$\begin{aligned} u(x,z,t) \quad &= \quad a\omega f(t) \frac{\cosh(k(z-h))}{\sinh(kh)} \cos(kx + \sigma t) \\ w(x,z,t) \quad &= \quad a\omega f(t) \frac{\sinh(k(z-h))}{\sinh(kh)} \sin(kx + \sigma t) \quad , \end{aligned} \tag{44}$$

where h is the height of the air above the free surface. Using this formulation, the horizontal water-particle velocity is discontinuous across the air-water interface, and the vertical water-particle velocity is continuous across the air-water interface.

Results

5365 geometry (Athena)

A three-dimensional numerical simulation that uses 850x192x128= 20,889,600 grid points, 5x8x4=160 subdomains, and 160 nodes has been performed on a Cray XT3. The length, width, depth, and height of the computational domain are respectively 4.0, 1.0, 1.0, 0.5 ship lengths (L_o). Grid stretching is employed in all directions. The smallest grid spacing is 0.0020 near the ship and mean waterline, and the largest grid spacing is 0.020 in the far field. The Froude number is $F_r = 0.4316$. Two incident wavelengths are considered: $\lambda = 1/2$ and $\lambda = 2$. In both cases, the wave steepness is $H/\lambda = 0.06$, where $H = 2a$ is the wave height. The equations for the wavemaker are imposed ahead of the ship over the range $1 \leq x \leq 1.5$. Initial transients are minimized by slowly ramping up the free-stream current and the incident wave amplitude. The period of adjustment is $T_o = 0.5$. For this simulation, the non-dimensional time step is Δt=0.0005. The numerical simulation runs 10,000 time steps corresponding to 5 ship lengths. Each simulation requires about 80 hours of wall-clock time. The numerical results are compared to experimental measurements that had been performed at the Naval Surface Warfare Center (Ratcliffe & Dommermuth 2007).

Figures 1 show perspective views of the predicted free-surface elevations at time $t = 5$ for the two cases. The color bar denotes free-surface elevations between -0.02 to 0.02 for the short-wave case and -0.04 to 0.04 for the long-wave case. The incident wave propagates from the inlet to the exit with no attenuation in amplitude. This indicates that the effects of numerical dissipation are minimal.

The predicted and measured free-surface elevations as a function of time at are shown in Figures 2. The predicted free-surface elevations are ramped up to their full height. This minimizes transients associated with starting up the numerical wavemaker. The measured free-

surface elevations show slight irregularities that are associated with limitations with the wavemaker at DTMB.

Figures 3 show the predicted vertical force compared to measurements. The displacement has been subtracted out from the results. As the model ramps up to full speed, a mean suction force is induced on the model. The oscillatory portion of the force is dominated by hydrostatics. For the short-wave case, the numerical predictions show slightly more sinkage than had been measured. The oscillatory portions of the forces agree well.

Figures 4 show the predicted drag force compared to measurements. In the case of the numerical simulations, the drag is initially zero because the model is ramped up to full speed from zero forward speed. The primary harmonics that are evident in the plots are due to the incident wave forces. We speculate that the higher harmonics that are evident in the laboratory results, which are especially evident for the longer wave, are due to vibrations in the structure that is used to restrain the model. Another possibility is the variation in the incident wave amplitude in the experiments. Structural vibrations could be assessed by installing accelerometers on the model. The variation in the incident wave amplitude could be accounted for in the numerical simulations by using wave-probe data as input. In general, numerical predictions and laboratory measurements agree well.

5514 and 5613 geometries

Forced-motion studies of models 5514 and 5613 have been performed. The models are forced to move in heave, pitch, and roll while moving with constant forward speed. The Froude number for both hull forms is $F_r = 0.3$. For the heave and pitch studies, a plane of symmetry is used on the centerplane of the computational domain. The heave and pitch simulations use 680x192x128=16,711,680 grid points and 4x8x4=128 sub-domains. The forced roll simulations use 680x384x128=33,423,360 grid points and 4x8x4=128 sub-domains. The length, width, depth, and height of the computational domain are respectively 3.0, 1.0, 1.0, 0.5 ship lengths (L_o) for the heave and pitch studies. The width of the domain is doubled for the roll simulations. All of the simulations use 128 processors on a Cray XT3. For model 5514, the full-scale length and forward speed are respectively $L_o = 142.0$m and $U_o = 11.20$m/s. For model 5613, $L_o = 154.0$m and $U_o = 11.66$m/s. Table 1 summarizes the non-dimensional amplitudes and frequencies of motion. The heave amplitudes correspond to ranges of motion that are 80% of the mean drafts. Table 2 summarizes the time step and the number of time steps. Smaller time steps are used for the roll simulations and one heave case due to Courant-stability considerations. Several animations of these simulations have been prepared at the flow visualization center at ERDC. The animations are accessible at http://www.saic.com/nfa/. This website also includes animations of the Athena moving with constant forward speed into head seas.

	5514		5613	
	amplitude	frequency	amplitude	frequency
Heave	0.3667	13.95	0.02857	14.53
Pitch	5°	13.95	5°	14.53
Roll	65°	8.525	65°	8.877

Table 1: Forced-motion parameters.

	5514		5613	
	Δt	N	Δt	N
Heave	0.0005	4,000	0.00025	10,000
Pitch	0.0005	4,000	0.0005	4,000
Roll	0.00025	8,000	0.00025	8,000

Table 2: Time step and number of time steps.

Conclusions

In terms of progress, it is interesting to consider the results of research reported in earlier ONR symposiums. Dommermuth et al. (1998) study the flow near the bow of model 5415 using a variable-density, cartesian-grid formulation. A body force is used by Dommermuth et al. (1998) to impose the body boundary condition. The numerical results of Dommermuth et al. (1998) barely capture the initial onset of wave overturning near the bow. Sussman & Dommermuth (2001) continue to develop interface capturing methods. Once again, comparisons are shown to the bow flow of model 5415. The results do not show significant improvement over their earlier results. However, their calculations of the breakup of a turbulent spray sheet illustrate a novel application of interface-capturing methods. Dommermuth et al. (2004) use two methods to study the flow around model 5415, a vertical strut, and a bluff wedge. The first method uses free-slip conditions on the hull in combination with a hybrid level-set and VOF interface-capturing method. In addition, adaptive mesh refinement (AMR) is used to improve grid resolution near the hull and free-surface interface. Their preliminary results illustrate the efficiency of AMR. The second method uses body-force and VOF formulations on a cartesian grid with no grid stretching. The results show more fine-scale detail than the earlier studies. The predicted free-surface elevations compare well with experiments, but the body-force method is too "sticky" because too much fluid is dragged with the ship hull. Based on these results, Dommermuth et al. (2006) use free-slip boundary conditions to impose the body boundary condition to reduce stickiness. The VOF algorithm is generalized to include free-slip conditions on the ship hull. The grid is stretched along the cartesian axes to

improve grid resolution. Numerical predictions compare well with laboratory measurements of ship models moving with constant forward speed. The present research implements forced motions and ambient waves. As the ship moves, the portion of the cartesian grid that is cut by the ship hull is continuously calculated. The inherent simplicity of the cartesian-grid formulation is retained even though the ship moves through the grid. Ambient waves are generated by forcing the flow in the water and the air based on analytic solutions for two-phase flows. The procedure is illustrated using regular waves, but it is general enough to model a seaway.

Acknowledgements

The Office of Naval Research supports this research under contract number N00014-07-C-0184. Dr. Patrick Purtell is the program manager. The David Taylor Model Basin under the guidance of Dr. Arthur Reed also supports this research. This work is supported in part by a grant of computer time from the DOD High Performance Computing Modernization Program (http://www.hpcmo.hpc.mil/). The numerical simulations have been performed on the Cray XT3 at the U.S. Army Engineering Research and Development Center (ERDC). The support of the flow visualization group at ERDC under the guidance of Paul Adams is gratefully acknowledged.

References

Carderock Division, Surface Ship Model 5415, Tech. rep., Naval Surface Warfare Center, 2005.
URL: *http://www.dt.navy.mil/hyd/sur-shi-mod/*

Colella, P., Graves, D., Modiano, D., Puckett, E., & Sussman, M., "An embedded boundary / volume of fluid method for free-surface flows in irregular geometries," Proceedings of FEDSM99, 3rd ASME/JSME Joint Fluids Engineering Conference, San Francisco, CA., 1999, pp. 1–6.

Dommermuth, D., "The initialization of vortical free-surface flows," J. Fluids Eng., Vol. 116, 1994, pp. 95–102.

Dommermuth, D., Innis, G., Luth, T., Novikov, E., Schlageter, E., & Talcott, J., "Numerical simulation of bow waves," Proceedings of the 22nd Symposium on Naval Hydrodynamics, Washington, D.C., 1998, pp. 508–521.

Dommermuth, D. G., "The initialization of nonlinear waves using an adjustment scheme," Wave Motion, Vol. 32, 2000, pp. 307–317.

Dommermuth, D. G., O'Shea, T. T., Wyatt, D. C., Sussman, M., Weymouth, G. D., Yue, D. K., Adams, P., & Hand, R., "The numerical simulation of ship waves using cartesian-grid and volume-of-fluid methods," Proceedings of the 26th Symposium on Naval Hydrodynamics, Rome, Italy, 2006, to appear.

Dommermuth, D. G., Sussman, M., Beck, R. F., O'Shea, T. T., Wyatt, D. C., Olson, K., & MacNeice, P., "The numerical simulation of ship waves using cartesian-grid methods with adaptive mesh refinement," Proceedings of the 25th Symposium on Naval Hydrodynamics, St. John's, Newfoundland and Labrador, Canada, 2004, pp. 1–17.

Gueyffier, D., Li, J., Nadim, A., Scardovelli, R., & Zaleski, S., "Volume-of-fluid interface tracking with smoothed surface stress methods for three-dimensional flows," J. Comp. Phys., Vol. 152, 1999, pp. 423–456.

Knupp, P. M. & Steinerg, S., Fundamentals of grid generation, CRC Press, Inc., 1993.

Leonard, B., "Bounded higher-order upwind multidimensional finite-volume convection-diffusion algorithms," W. Minkowycz & E. Sparrow, eds., Advances in Numerical Heat Transfer, Taylor and Francis, Washington, D.C., 1997, pp. 1–57.

Mampaey, F. & Xu, Z.-A., "Simulation and experimental validation of mould filling," Modeling of Casting, Welding and Advanced Solidification Processes VII, London, England, 1995, pp. 10–12.

Orlanski, I., "A simple boundary condition for unbounded hyperbolic flows," J. Comp. Phys., Vol. 21, 1976, pp. 251–269.

Pilliod, J. & Puckett, E., Second-Order Accurate Volume-of-Fluid Algorithms for Tracking Material Interfaces, Technical Report LBNL–40744, Lawrence Berkeley National Laboratory, 1997.

Puckett, E., Almgren, A., Bell, J., Marcus, D., & Rider, W., "A second-order projection method for tracking fluid interfaces in variable density incompressible flows," J. Comp. Physics, Vol. 130, 1997, pp. 269–282.

Ratcliffe, T. & Dommermuth, D. G., "Experimental wave loads and numerical predictions obtained on model-scale hull form of the u.s. navy research vessel athena," Proceedings of the 2nd International Conference on Marine Research and Transportation, Napoli, Italy, 2007, to appear.

Rider, W., Kothe, D., Mosso, S., Cerutti, J., & Hochstein, J., "Accurate solution algorithms for incompressible multiphase flows," AIAA paper 95–0699.

Sussman, M., "A second order coupled level set and volume-of-fluid method for computing growth and collapse of vapor bubbles," J. Comp. Phys., Vol. 187, 2003a, pp. 110–136.

Sussman, M. & Dommermuth, D., "The numerical simulation

of ship waves using cartesian-grid methods," Proceedings of the 23rd Symposium on Naval Ship Hydrodynamics, Nantes, France, 2001, pp. 762–779.

Wilson, W., Fu, T., Pence, A., & Gorski, J., "The measured and predicted wave field of model 5365: an evaluation of current cfd capability," Proceedings of the 26th Symposium on Naval Hydrodynamics, Rome, Italy, 2006, to appear.

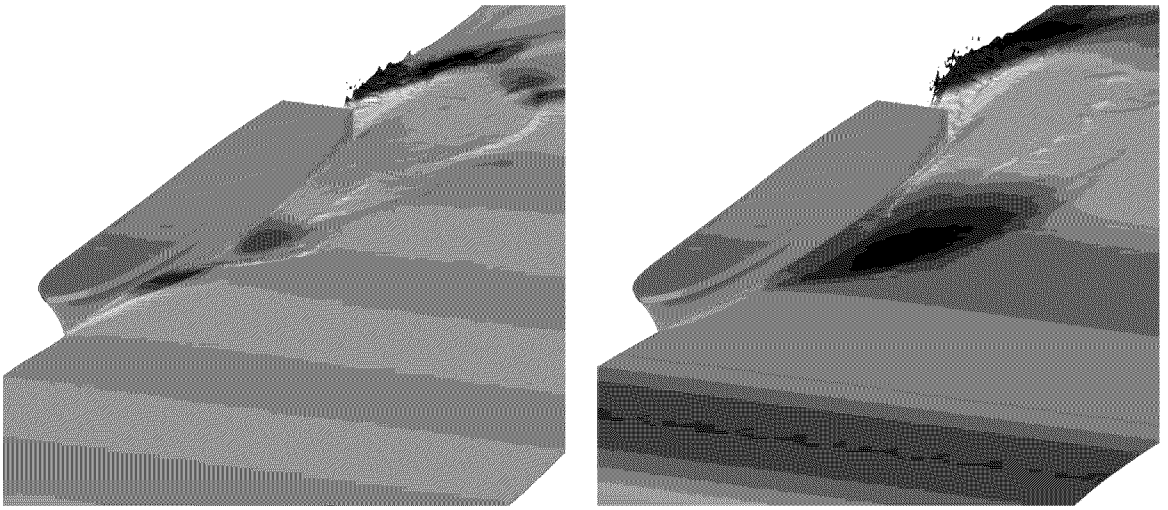

(a) $\lambda = \frac{1}{2}$ (b) $\lambda = 2$

Figure 1: Model 5365 (Athena) perspective view of the free surface.

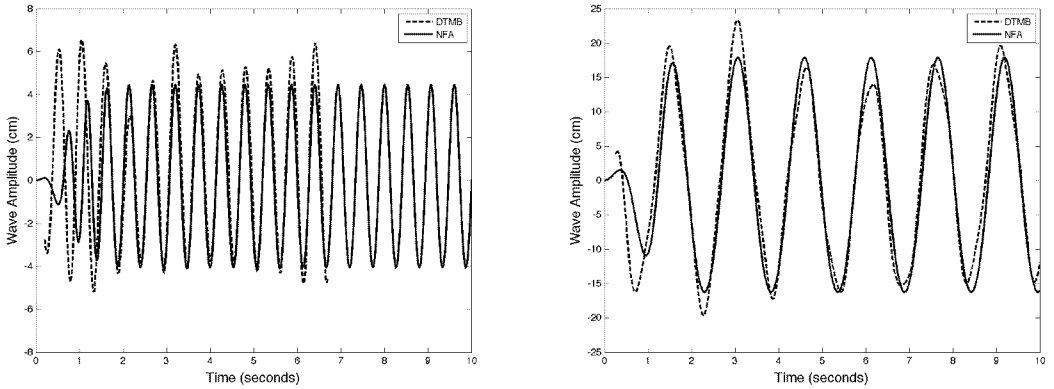

(a) $\lambda = \frac{1}{2}$ (b) $\lambda = 2$

Figure 2: Model 5365 (Athena) wave elevation at $x = 1.5$.

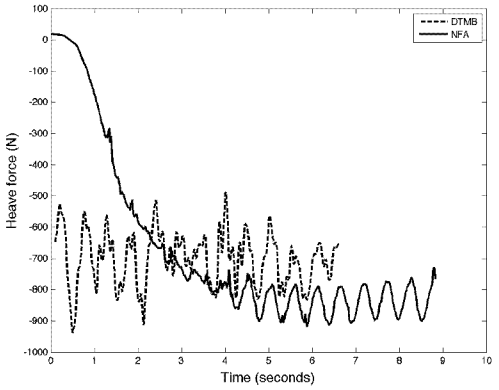

(a) $\lambda = \frac{1}{2}$

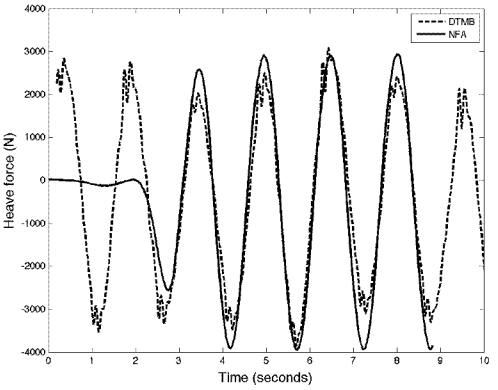

(b) $\lambda = 2$

Figure 3: Model 5365 (Athena) vertical forces.

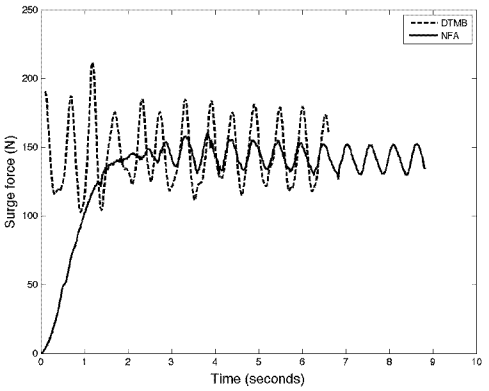

(a) $\lambda = \frac{1}{2}$

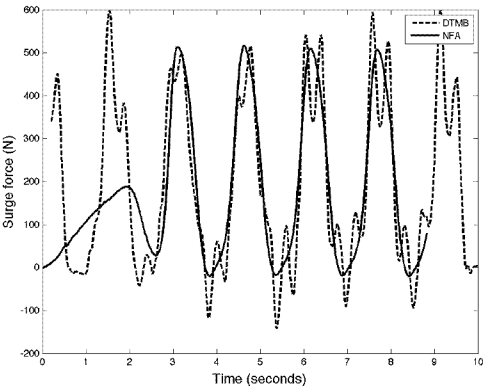

(b) $\lambda = 2$

Figure 4: Model 5365 (Athena) drag forces.